CrossMark

ORIGINAL PAPER

Hexagram-like CoS-MoS$_2$ composites with enhanced activity for hydrogen evolution reaction

Xuan Shen[1] · Xiaohong Xia[1] · Weichun Ye[1] · Yongling Du[1] · Chunming Wang[1]

Abstract Hexagram-like CoS-MoS$_2$ composites were prepared on indium tin oxide (ITO) conductive glasses via cyclic voltammetry electrodeposition using Co(NO$_3$)$_2$ and (NH$_4$)$_2$MoS$_2$ as precursors and tested for application in hydrogen evolution reaction (HER). The structure of CoS-MoS$_2$ composites was characterized by X-ray diffraction (XRD), scanning electron microscope (SEM), and X-ray photoelectron spectrum (XPS). Electrochemical characterizations indicate that CoS-MoS$_2$ composites exhibit more excellent catalytic activity and stability than MoS$_2$. Compared with pure MoS$_2$, the hexagram-like CoS-MoS$_2$ composites with increased specific surface area improved the density of exposed active sites, and the Co binding S edges in CoS-MoS$_2$ composites promote the number of highly catalytic edge sites and decreased the binding energy $\triangle G_H$. Moreover, the effects of different substrates on the CoS-MoS$_2$ composites were also investigated. Our further understanding of this highly active hydrogen evolution catalyst can facilitate the development of economical electrochemical hydrogen production systems.

✉ Chunming Wang
wangcm@lzu.edu.cn

[1] College of Chemistry and Chemical Engineering, Lanzhou University, Lanzhou 730000, People's Republic of China

Introduction

Hydrogen energy is considered as one of the ideal candidates for replacing fossil fuels in the future, because of its numerous advantages, such as recyclability, free pollution, and high efficiency [1, 2]. Direct electrochemical splitting of water is currently the simplest way to generate hydrogen of high purity at the most economical price and has attracted considerable attention [3, 4]. Noble platinum (Pt) metal exhibits excellent electrocatalytic activity and low overpotential for HER, but its high cost and resource scarcity make it difficult to achieve large scale application. Therefore, developing an inexpensive, highly catalytic active, stable HER electrocatalysts to replace Pt is highly desirable [5–7].

Over the last few years, MoS$_2$ has been considered as promising alternatives for noble metals due to its earth abundance composition and excellent HER activity [8]. As previous studies reported, the HER activity originates from the unsaturated sulfur edges of MoS$_2$ [9]. As a result, much effort has been made to prepare MoS$_2$ nanostructures with more exposed sulfur edges, leading to high HER activity [10–13]. Introducing promoter atoms such as Co or Ni to MoS$_2$ also promote its HER activity greatly [14, 15]. This enhancement may involve morphology changes or chemical changes with the possibility of creating novel bimetallic active sites with sulfur bridging [16–18]. The morphology is an essential issue to design efficient MoS$_2$ catalyst. An ideal morphology with more specific surface area increases exposed active sites, resulting in more efficient activity for HER. In addition, the improvement of the inherent activity of MoS$_2$ catalyst is equally important. The incorporation of Co or Ni into MoS$_2$ can tune the intrinsic catalytic activity due to their specific coupling with S edges [19]. And the presence of Co binding S edges can reduce the binding energy of hydrogen from 0.18 to 0.10 eV [20, 21]. Furthermore, it is reported that cobalt

sulfides are efficient and robust HER catalysts [22]. It is thus expected that CoS-MoS$_2$ composites could exhibit greatly enhanced activity for HER.

MoS$_2$-based catalysts normally prepared via sulfurization of mixtures of molybdates with oxides of the metallic promoter [18]. This synthesis process involves the high temperature and toxic H$_2$S co-procedure and always requires a large investment in equipment, which hamper its wide range of application [19]. However, electrodeposition method has been proven to be a more suitable method for preparing catalysts. The synthesis technique avoids these harsh conditions and is performed by simple solution electrochemistry under ambient conditions. During the process, the deposition graph can reflect the growth situation of catalysts. Moreover, the catalyst is directly electrodeposited onto electrode surfaces, which eliminates the immobilization step. As a result, these catalysts prepared by electrodeposition are easy to make, less costly, and amenable to broaden application.

In this paper, we report a facile one-step electrodeposition of CoS-MoS$_2$ composites on ITO with Co(NO$_3$)$_2$ and (NH$_4$)$_2$[MoS$_4$] as precursors. The results show the presence of CoS in CoS-MoS$_2$ composites enhances the catalytic activity. As a HER electrocatalyst, the CoS-MoS$_2$ catalyst exhibits superior activity than MoS$_2$ and displays good stability.

Subsequently, CoS-MoS$_2$ composites deposited on polyimide/reduced graphene oxide (PI/RGO) and polyimide/reduced graphene oxide-carbon nanotube (PI/RGO-CNT) were done for comparison.

Experimental

Materials

Co(NO$_3$)$_2$·6H$_2$O and (NH$_4$)$_2$MoS$_2$ were purchased from Beijing J&K Scientific Ltd. (Beijing, China). Graphite, 4, 4′-oxydianiline (ODA), and 4, 4′-oxydiphthalic anhydride (ODPA) were purchased from Shanghai Chemical Co. Ltd. (Shanghai, China). CNT was obtained from Chengdu Organic Chemicals Co. Ltd. (Chengdu, China). All reagents in this experiment were used as received without further purification except N-methyl pyrrolidone (NMP) was re-distilled. Deionized water was used throughout this study.

Preparation of CoS-MoS$_2$ composite

The cyclic voltammetry (CV) was performed for the electrochemical deposition of CoS-MoS$_2$ composites, and the

Fig. 1 SEM images of **a** MoS$_2$ deposited on ITO and CoS-MoS$_2$ deposited on ITO with different deposition cycles: **b** 5, **c** 15, and **d** 25
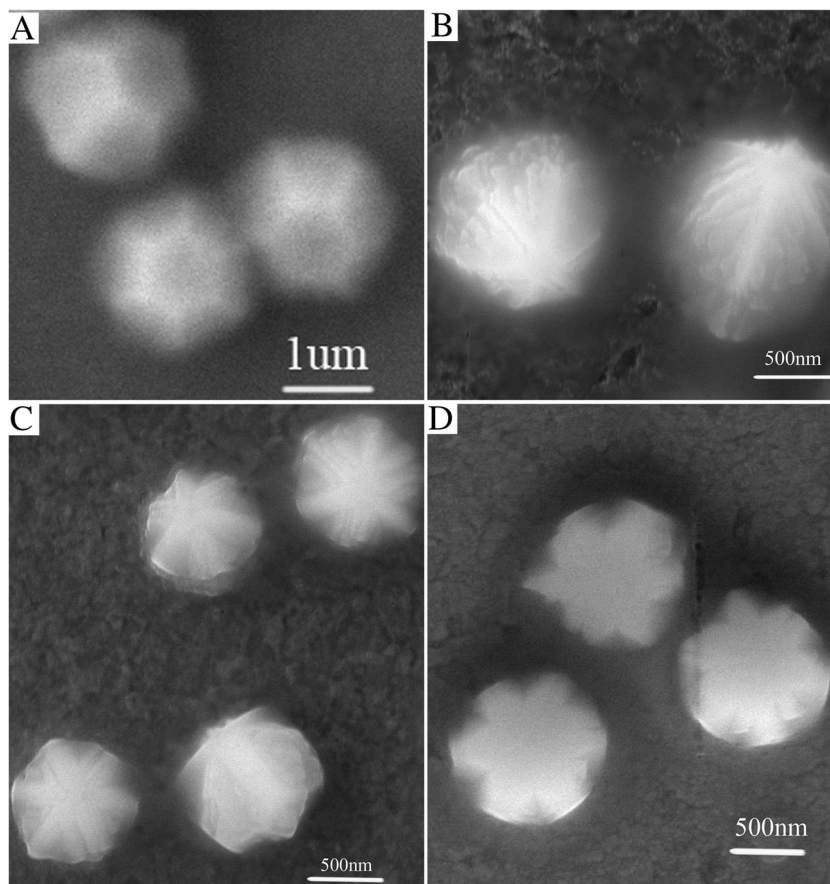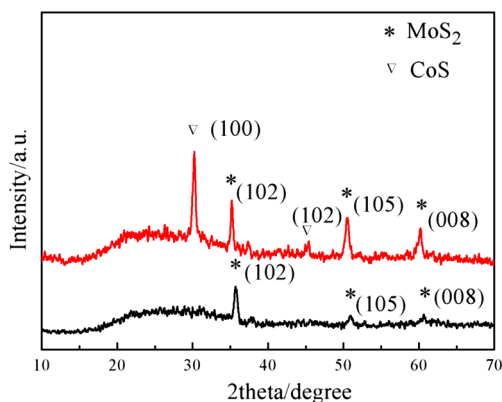
Fig. 2 XRD patterns of MoS_2 (curve a) and $CoS-MoS_2$ (curve b) deposited on ITO

potential from −1.0 to 0.1 V vs. SCE was applied with a scan rate of 50 mV s^{-1} for different cycles [14]. The deposition solution was simply composed of $NaClO_4$ (0.1 M), $(NH_4)_2[MoS_4]$ (2 mM), and $Co(NO_3)_2$ (2 mM). A CHI660C electrochemical workstation (CH Instrument, USA) with conventional three-electrode system was employed in the work. The catalysts were deposited on three different types of electrodes: ITO, PI/RGO, and PI/RGO-CNT. A saturated calomel electrode (SCE) and a Pt wire auxiliary electrode were used as reference electrode and counter electrode, respectively. For comparison, pure MoS_2 was also deposited in a similar electrodeposition procedure without adding $Co(NO_3)_2$ into the deposition solution.

Fig. 3 XPS spectra of MoS_2 and $CoS-MoS_2$ composite deposited on ITO. **a** XPS Mo 3D spectra and **b** XPS S 2p spectra of MoS_2, **c** XPS Mo 3D spectra, **d** XPS S 2p spectrum, and **e** XPS Co 2p spectra of $CoS-MoS_2$
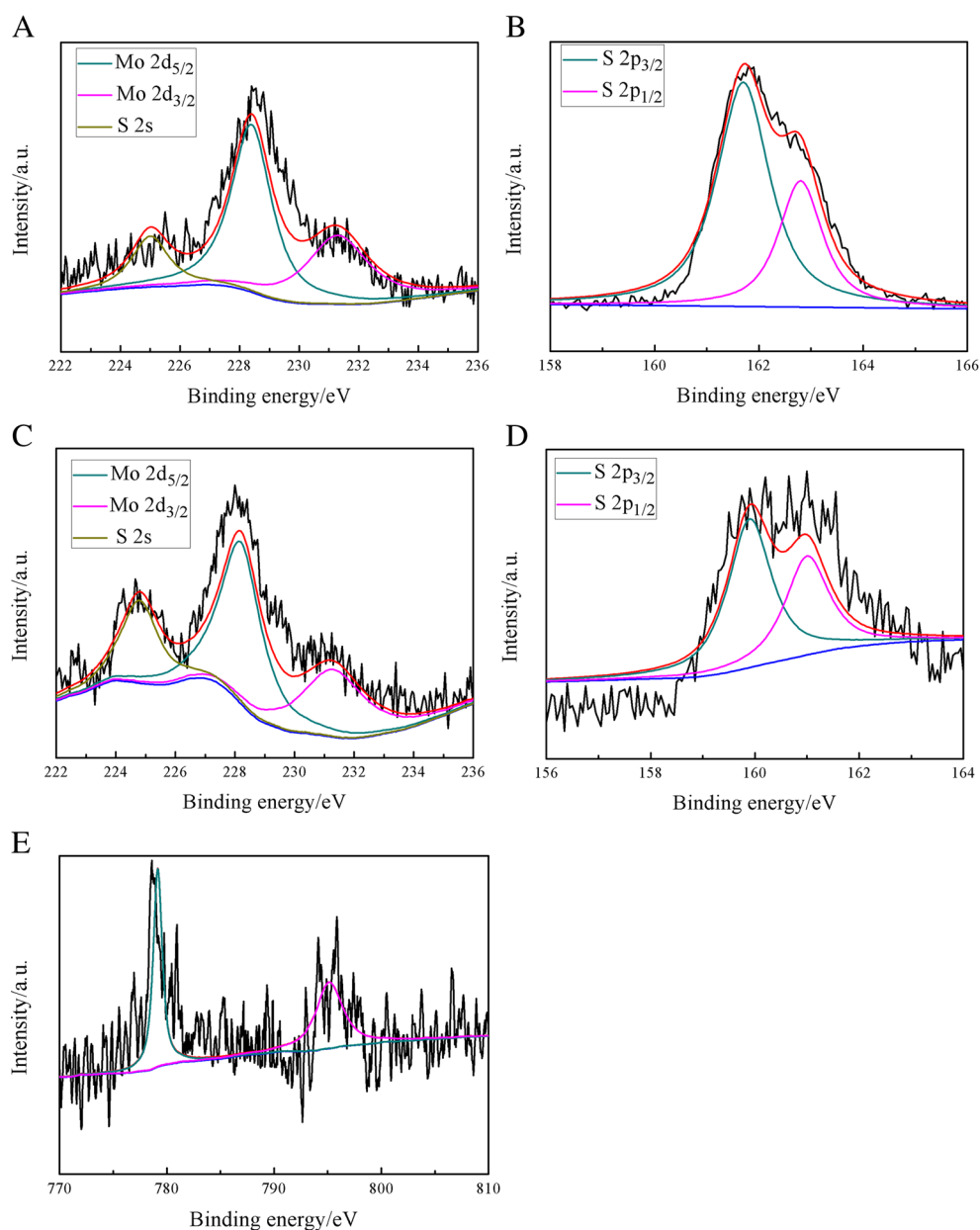
Synthesis of PI/RGO and PI/RGO-CNT polymer film

The graphene oxide (GO) was prepared by the modified Hummers method [23]. Then the obtained GO was reduced in hydrazine hydrate solution at 90 °C for 6 h to get the expected reduced graphene oxide (RGO) powder. The 0.2 g ODA and 0.3 g ODPA were putted into 25-mL flask, then dissolved them with 4 mL redistilled NMP with the protection of N_2. After stirred for 24 h, a polyamide acid (PAA) solution was obtained. Then 45 mg of RGO was exfoliated in PAA solution by ultrasonication technique for 8 h to form homogeneous black PAA/RGO turbid liquid. Finally, the PAA/RGO solution was dropped on ITO substrate and heated from room temperature to 300 °C, and PI/RGO polymer film was obtained.

PI/RGO-CNT polymer film was obtained through a similar method with 22.5 mg RGO and 22.5 mg CNT in PAA solution.

Characterization

The morphologies were investigated using field emission scanning electron microscopy (FE-SEM) (Kevex JSM-6701F, Japan). The crystalline structure was determined by X-ray diffraction (XRD) (RigakuD/max-2400). X-ray photoelectron spectrum (XPS) analysis was performed on an ESCALAB 210 instrument.

Results and discussion

Characterization of CoS-MoS$_2$ composite

The morphologies of MoS$_2$ and CoS-MoS$_2$ deposited on ITO were characterized by SEM. Figure 1a is the SEM image of MoS$_2$ catalysts, which displays regular tetrakaidecahedron and uniform distribution. Figure 1b–d show the SEM images of CoS-MoS$_2$ composites with different scan cycles: 5, 15, and 25, which indicate that various shapes of products were achieved by changing deposition time. As shown in Fig. 1b, the microspheres with snowflake structure were formed. At the deposited time of 15 cycles, the CoS-MoS$_2$ composites presented microspheres with hexagram structure. When the deposition time increased to 25 cycles, hexagram-like CoS-MoS$_2$ catalysts were clearly observed. The SEM images shown in Fig. 1b–d present that the morphology of CoS-MoS$_2$ composites changed from microsphere to hexagram
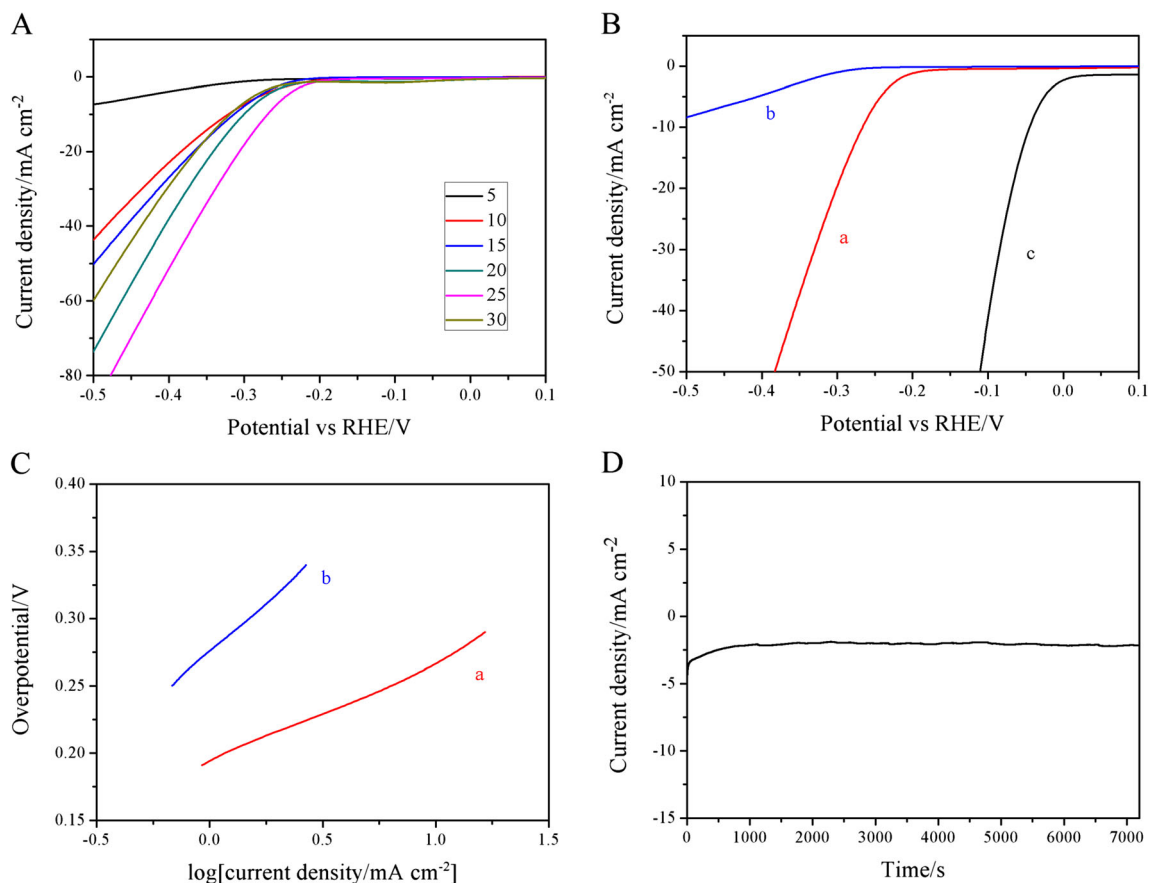

Fig. 4 **a** Polarization curves of CoS-MoS$_2$ with different deposition cycles in 0.5 M H$_2$SO$_4$: 5, 10, 15, 20, 25, and 30. **b** Polarization curves of CoS-MoS$_2$ (curve a), MoS$_2$ (curve b) deposited on ITO, and of Pt (curve c) in 0.5 M H$_2$SO$_4$. **c** Tafel plots of CoS-MoS$_2$ (curve a) and MoS$_2$ (curve b) deposited on ITO in 0.5 M H$_2$SO$_4$. **d** Durability test for CoS-MoS$_2$ deposited on ITO
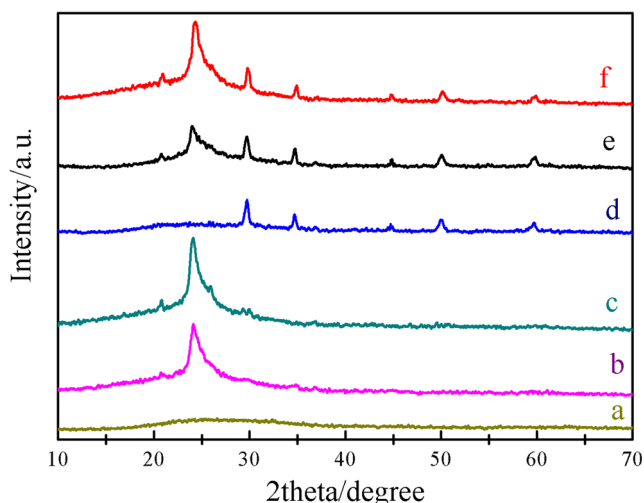
Fig. 5 XRD patterns of ITO (curve a), PI/RGO (curve b), PI/RGO-CNT (curve c), and CoS-MoS$_2$ composites deposited on different substrates: ITO (curve d), PI/RGO (curve e), and PI/RGO-CNT (curve f)

with the deposition progressing. According to previous theoretical and experimental results, the HER activity relates closely to the reactive edge density of the MoS$_2$, and increasing the number of exposed active edges is an efficient way to enhance the HER activity [9]. Compared with regular tetrakaidecahedron MoS$_2$, the hexagram-like CoS-MoS$_2$ composites with increased specific surface area expose more active edges, which were verified by electrochemical capacitance surface area measurements in Fig. 4d, thus, the CoS-MoS$_2$ composites show greater advantages for HER.

Figure 2 shows the XRD patterns of MoS$_2$ and CoS-MoS$_2$ deposited on ITO. For the as-prepared MoS$_2$, it is interesting to observe the (002) diffraction peak at 14° disappears; only three diffraction peaks corresponding to (102), (105), and (008) faces of MoS$_2$ are shown (JCPDS Card No. 37-1492). The XRD pattern of the CoS-MoS$_2$ composites exhibits all diffraction peaks related to the as-prepared MoS$_2$. The diffraction peaks located at 30.6° and 46.9° corresponds to (100) and (102) planes of CoS, respectively, (JCPDS Card No. 65-3418). In addition, the diffraction peak corresponding to the (102) plane of MoS$_2$ shifts to a lower angle in the CoS-MoS$_2$ composite, suggesting an interlayer distance increases in the direction [24].
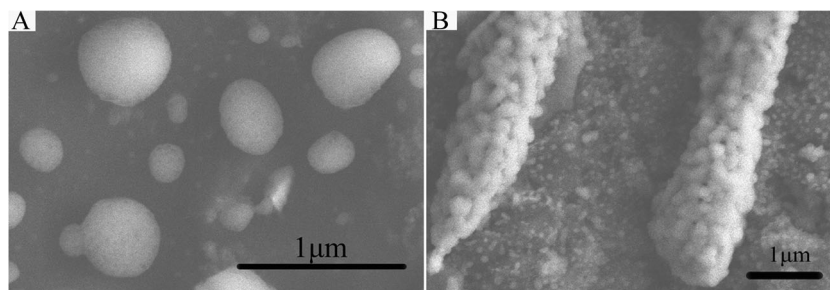
The chemical states of Mo and S were further investigated by X-ray photoelectron spectroscopy (XPS). As observed in Fig. 3a and c, the characteristic peaks located at 228.2 and 231.4 eV are attributed to Mo 3d$_{5/2}$ and Mo 3d$_{3/2}$, respectively, which indicates a + 4 oxidation state for the Mo. The peak with a binding energy at 225.2 eV corresponds to S 2 s [25]. Peaks corresponding to S 2p$_{3/2}$ and S 2p$_{1/2}$ of divalent sulfide ions (S^{2-}) are revealed at 161.5 and 162.6 eV. These results prove the composites contain MoS$_2$ [26]. Whereas the Co 2p region in Fig. 3e exhibits doublet bands at 779.0 and 795.0 eV, indicating the presence of Co^{2+} in the composites [27–29]. The results further verify the CoS-MoS$_2$ composites have been successfully prepared.

Electrochemical performance of MoS$_2$ and CoS-MoS$_2$ deposited on ITO

The linear scan voltammetry (LSV) measurements were used to test HER properties with a scan rate of 100 mV s^{-1} in 0.5 M H$_2$SO$_4$. Scan cycles during the electrodeposition process were designed to investigate their effects on catalytic activity, as shown in Fig. 4a. In the initial 25 scan cycles, the HER activity of CoS-MoS$_2$ increases with the number of scan cycles. However, at 30 scan cycles, the CoS-MoS$_2$ shows lower HER activity, indicating that the catalytic activity approaches saturation with about 25 scans cycles. Figure 4b shows the polarization curves of CoS-MoS$_2$ and MoS$_2$ deposited on ITO measured by LSV with correction for uncompensated *IR* drops (supporting information). The CoS-MoS$_2$/ITO exhibits a small onset overpotential of 0.19 V, which is more positive than that of MoS$_2$/ITO (0.24 V). Besides, at the same overpotential, CoS-MoS$_2$ catalysts show significantly higher HER current densities than MoS$_2$ catalysts. These results indicate that CoS-MoS$_2$ catalysts show enhanced HER activity over MoS$_2$ catalysts.

Tafel slope is often utilized to indicate the dominant mechanism involved in the HER process. The linear regions of the Tafel plots are fit into the Tafel equation ($\eta = b\log(j) + a$, where b is the Tafel slope).

In acid solutions, three principal reactions are assumed to predominate when hydrogen is evolved on a metal catalyst,
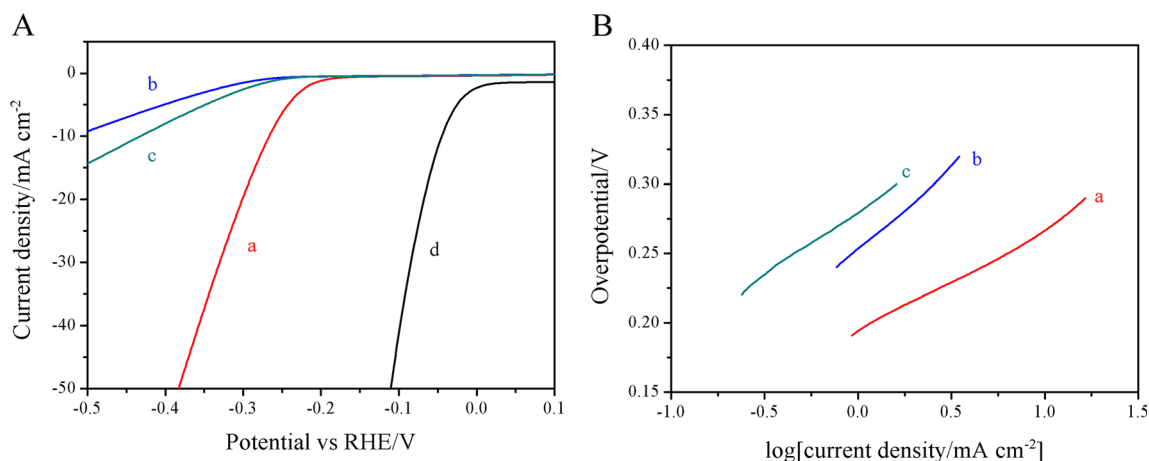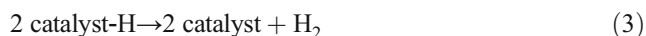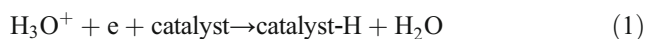
Fig. 6 SEM images of CoS-MoS$_2$ composites deposited on different substrates: **a** PI/RGO and **b** PI/RGO-CNT

Fig. 7 **a** Polarization curves of CoS-MoS$_2$ composites deposited on ITO (curve a), PI/RGO (curve b), PI/RGO-CNT (curve c), and of Pt (curve d) in 0.5 M H$_2$SO$_4$. **b** Tafel plots of CoS-MoS$_2$ deposited on ITO (curve a), PI/RGO (curve b), and PI/RGO-CNT (curve c) in 0.5 M H$_2$SO$_4$

commonly named the Volmer [Eq. (1)], Heyrovsky [Eq. (2)], and Tafel reactions [Eq. (3)].

$$H_3O^+ + e + catalyst \rightarrow catalyst-H + H_2O \qquad (1)$$

$$H_3O^+ + e + catalyst-H \rightarrow catalyst + H_2 + H_2O \qquad (2)$$

$$2 \text{ catalyst-H} \rightarrow 2 \text{ catalyst} + H_2 \qquad (3)$$

The Tafel slope is an inherent property of the catalyst. As shown in Fig. 4d, the Tafel slopes for MoS$_2$ and CoS-MoS$_2$ deposited on ITO are 101 and 74 mV dec^{-1}, respectively. The Tafel slope for CoS-MoS$_2$/ITO is much lower than that for MoS$_2$/ITO, suggesting the presence of CoS in CoS-MoS$_2$ composites enhances the HER activity. For MoS$_2$, active sites for HER are edge planes with unsaturated sulfur atoms [9]. The S edges are catalytically inactive sites, but the Co binding S edges in CoS-MoS$_2$ composites are catalytically active [19]. Another possible reason could be the decrease of the binding energy $\triangle G_H$ [20, 21].

The excellent stability of catalyst is another vital criterion to consider for commercial applications. We thus examined the durability of the CoS-MoS$_2$/ITO catalyst by potentiostatic measurements for 7200 s at −0.5 V vs. SCE in 0.5 M H$_2$SO$_4$, as shown in Fig. 4d. The current density has a slight current loss after 7200 s, which may be due to some modification of the surface state of the catalyst [30], suggesting that this catalyst has good stability in acidic electrolyte.

Electrochemical performance of CoS-MoS$_2$ composites on different substrates

We further deposited CoS-MoS$_2$ on PI/RGO and PI/RGO-CNT, and the effects of different substrates on CoS-MoS$_2$ composites were also investigated.

Figure 5 shows the XRD patterns of all bare substrates and CoS-MoS$_2$ deposited on ITO, PI/RGO, and PI/RGO-CNT. The XRD patterns of CoS-MoS$_2$ deposited on ITO, PI/RGO,
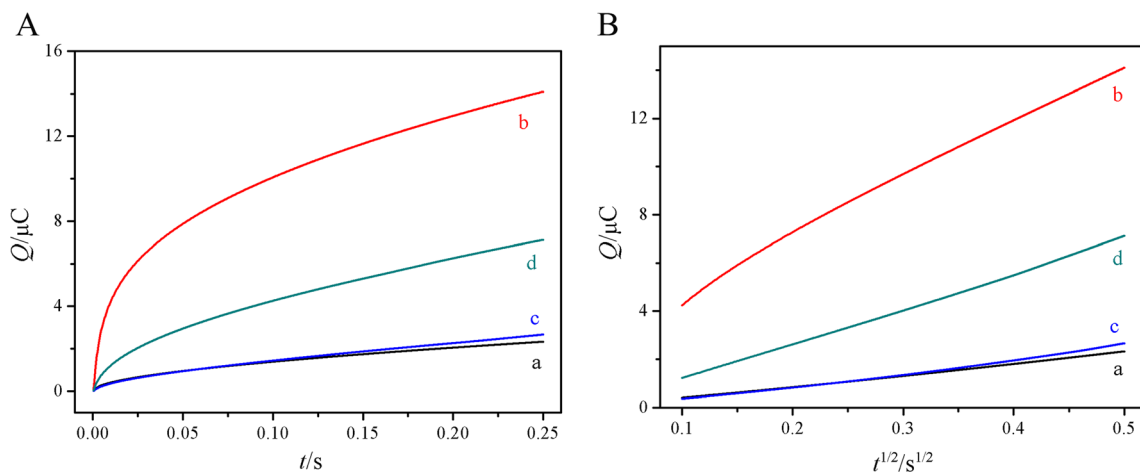

Fig. 8 **a** Polts of Q–t curves of MoS$_2$/ITO (curve a), CoS-MoS$_2$/ITO (curve b), CoS-MoS$_2$/PI/RGO (curve c), and CoS-MoS$_2$/PI/RGO-CNT (curve d) in 0.1 mM K$_3$[Fe(CN)$_6$] containing 1.0 M KCl. **b** Plot of Q–$t^{1/2}$ curves of MoS$_2$/ITO (curve a), CoS-MoS$_2$/ITO (curve b), CoS-MoS$_2$/PI/RGO (curve c), and CoS-MoS$_2$/PI/RGO-CNT (curve d)

Table 1 Comparison of MoS$_2$-based electrocatalysts explored towards the HER

Catalyst	Electrode/Supporting material	Electrolyte	HER onset (mV)	Tafel slope (mV dec^{-1})	Ref.
MoS$_2$	Au(111)	0.5 M H$_2$SO$_4$	~ − 150	55–60	[34]
MoS$_2$ nanosheets	GC	0.5 M H$_2$SO$_4$	~ − 150 to 200	70	[35]
2D MoS$_2$ nanosheets	GC	0.5 M H$_2$SO$_4$	~480	40	[36]
2D MoS$_2$ nanosheets	EPPG	0.5 M H$_2$SO$_4$	~ − 450	74	[36]
2D MoS$_2$ nanosheets	BDD	0.5 M H$_2$SO$_4$	~ − 450	90.9	[36]
2D MoS$_2$ nanosheets	SPE	0.5 M H$_2$SO$_4$	~ − 440	92	[36]
Ni$_x$S$_y$-MoS$_2$ hybrid microspheres	GC	0.5 M H$_2$SO$_4$	~ − 160	55.6	[37]
CoS-MoS$_2$	ITO	0.5 M H$_2$SO$_4$	~ − 190	74	This work
CoS-MoS$_2$	PI/RGO	0.5 M H$_2$SO$_4$	~ − 230	93	This work
CoS-MoS$_2$	PI/RGO-CNT	0.5 M H$_2$SO$_4$	~ − 220	85	This work

Key: *GC* glassy carbon, *EPPG* edge plane pyrolytic graphite, *BDD* boron doped diamond, *SPE* screen-printed graphite electrode, *ITO* indium tin oxide, *PI/RGO* polyimide/reduced graphene oxide, *PI/RGO-CNT* polyimide/reduced graphene oxide-carbon nanotube

and PI/RGO-CNT have peaks at the same position, except the diffraction peak around 20° and 25°. The PI film has a diffraction peak at 20°, and the diffraction peak around 25° is attributed to the (002) plane of the RGO and the CNT [31, 32]. The result confirms the CoS-MoS$_2$ composites deposited on ITO, PI/RGO, and PI/RGO-CNT was prepared successfully.

The morphologies of CoS-MoS$_2$ composites deposited on PI/RGO and PI/RGO-CNT were characterized by SEM shown in Fig. 6. The presence of polymer film resulted in an appreciable change to the morphology of the CoS-MoS$_2$ composites on ITO, suggesting the substrates influence the growth of the CoS-MoS$_2$ composites.

The highly catalytic activity is demonstrated by comparing the current densities of CoS-MoS$_2$ catalysts deposited on ITO, PI/RGO, and PI/RGO-CNT. As shown in Fig. 7a, for achieving a catalytic current density of 10 mA cm^{-2}, the overpotentials need to be 0.27, 0.52, and 0.43 V for CoS-MoS$_2$ deposited on ITO, PI/RGO, and PI/RGO-CNT, respectively. At the same overpotential, CoS-MoS$_2$/ITO catalysts exhibit higher HER current densities than CoS-MoS$_2$/PI/RGO and CoS-MoS$_2$/PI/RGO-CNT catalysts. From Fig. 7b, the Tafel slopes for CoS-MoS$_2$ deposited on ITO, RGO, and RGO-CNT are 74, ~93, and ~85 mV dec^{-1}, respectively.

The electrochemically effective surface area (A) of electrode can be determined by chronocoulometry using 0.1 mM K$_3$[Fe(CN)$_6$] as model complex based on Anson equation [33]:

$$Q(t) = 2nFAC\left(\frac{Dt}{\pi}\right)^{\frac{1}{2}} + Q_{dl} + Q_{ads}$$

where C is the concentration of substrate, D is the diffusion coefficient, taking a value of 7.6×10–6 cm^2 s^{-1} (25 °C) in 0.1 mM K$_3$[Fe(CN)$_6$] containing 1 M KCl, Q_{dl} is the double layer charge, and Q_{ads} is the Faradic charge. Figure 8a shows the plots of Q-t for the MoS$_2$/ITO, CoS-MoS$_2$/ITO, CoS-MoS$_2$/PI/RGO, and CoS-MoS$_2$/PI/RGO-CNT. Based on the slope of Q-$t^{1/2}$ shown in Fig. 8b, A is calculated to be 0.163 cm^2 for MoS$_2$/ITO; while the CoS-MoS$_2$/ITO owns the electrochemically effective surface area as high as 0.778 cm^2. For comparison, the electrochemically effective surface areas of CoS-MoS$_2$/PI/RGO and CoS-MoS$_2$/PI/RGO-CNT are 0.195 and 0.491 cm^2, respectively. The ratios of the electrochemically effective surface area to geometric area (0.1256 cm^2) of MoS$_2$/ITO, CoS-MoS$_2$/ITO, CoS-MoS$_2$/PI/RGO, and CoS-MoS$_2$/PI/RGO-CNT are 1.30, 6.19, 1.55, and 3.91, respectively.

Table 1 presents a literature overview of MoS$_2$-based electrocatalysts explored towards the HER. It is evident that MoS$_2$ have shown promising advantages as a HER catalyst. The incorporation of CoS greatly improves the performance of MoS$_2$.

Conclusion

In summary, hexagram-like CoS-MoS$_2$ composites have been first successfully electrodeposited on ITO via cyclic voltammetry electrodeposition with (NH$_4$)$_2$[MoS$_2$] and Co(NO$_3$)$_2$ as precursors with the ratio of 2:1. The results demonstrate that hexagram-like CoS-MoS$_2$ composites exhibit more outstanding catalytic activity and better stability for HER than pure MoS$_2$ and spherical CoS-MoS$_2$ composites in acid solution. The excellent electrocatalytic performance could be ascribed mainly to following origins: The obtained hexagram-like CoS-MoS$_2$ composites increase its specific surface area, which improves the number of exposed active edges, in remarkable contrast with the traditional MoS$_2$ and spherical CoS-MoS$_2$ composites, and the presence of CoS converts catalytically inactive sites S edges into the Co binding S edges with catalytic activity and decreases the binding energy $\triangle G_H$.

In other word, the incorporation of CoS changes both the morphology of MoS₂ and the intrinsic activity of MoS₂. Furthermore, the CoS-MoS₂ composites were prepared on different substrates, and the results indicate that the substrates influence the growth of the CoS-MoS₂ composites. This catalyst made of relatively cheap and abundant elements with highly activity and stability for HER in acid solution, the CoS-MoS₂ composite as a promising candidate material will enable the widespread deployment of cost-effective systems for electrochemical hydrogen production.

References

1. Greeley J, Jaramillo TF, Bonde J, Chorkendorff I, Nørskov JK (2006) Computational high-throughput screening of electrocatalytic materials for hydrogen evolution. Nat Mater 5:909–913

2. Walter MG, Warren EL, McKone JR, Boettcher SW, Boettcher QX, Santori EA, Lewis NS (2010) Solar water splitting cells. Chem Rev 110:6446–6473

3. Nowotny TJ, Rekas M, Sorrell CC (2002) Photo-electrochemical hydrogen generation from water using solar energy. Int J Hydrog Energy 27:991–1022

4. Lv XJ, Fu WF, Chang HX, Zhang H, Cheng JS, Zhang GJ, Song Y, Hu CY, Li JH (2012) Hydrogen evolution from water using semiconductor nanoparticle/graphene composite photocatalysts without noble metals. J Mater Chem 22:1539–1546

5. Lu Z, Zhang H, Zhu W, Yu X, Kuang Y, Chang Z, Lei X, Sun X (2013) In situ fabrication of porous MoS₂ thin-films as high-performance catalysts for electrochemical hydrogen evolution. Chem Commun 49:7516–7518

6. Subbaraman R, Tripkovic D, Strmcnik D, Chang KC, Uchimura M, Paulikas AP, Stamenkovic V, Markovic NM (2011) Enhancing hydrogen evolution activity in water splitting by tailoring Li⁺-Ni(OH)₂-Pt interfaces. Science 334:1256–1260

7. Xu Y, Gao M, Zheng Y, Jiang J, Yu S (2013) Nickel/nickel(II) oxide nanoparticle anchored onto cobalt(IV) diselenide nanobelts for the electrochemical production of hydrogen. Angew Chem Int Ed 52: 5846–5859

8. Xie J, Zhang H, Li S, Wang R, Sun X, Zhou M, Zhou J, Lou X, Xie Y (2013) Defect-rich MoS₂ ultrathin nanosheets with additional active edge sites for enhanced electrocatalytic hydrogen evolution. Adv Mater 25:5807–5813

9. Benck JD, Chen ZB, Kuritzky LY, Forman AJ, Jaramillo TF (2012) Amorphous molybdenum sulfide catalysts for electrochemical hydrogen production: insights into the origin of their catalytic activity. ACS Catal 2:1916–1923

10. Chang Y, Lin C, Chen Z, Hsu C, Lee Y, Zhang W, Wei K, Li L (2013) Highly efficient electrocatalytic hydrogen production by MoSₓ grown on graphene-protected 3D Ni foams. Adv Mater 25: 756–760

11. Zhuo S, Xu Y, Zhao W, Zhang J, Zhang B (2013) Hierarchical nanosheet-based MoS₂ nanotubes fabricated by an anion-exchange reaction of MoO₃-amine hybrid nanowires. Angew Chem Int Ed 125:8602–8604

12. Wu Z, Fang B, Wang Z, Wang C, Liu Z, Liu F, Wang W (2013) A. Alfantazi, D. Wang, D.Wilkinson, MoS₂ nanosheets: a designed

13. Yan Y, Ge X, Liu Z, Wang J, Lee J, Wang X (2013) Facile synthesis of low crystalline MoS₂ nanosheet-coated CNTs for enhanced hydrogen evolution reaction. Nanoscale 5:7768–7771

14. Merki D, Vrubel H, Rovelli L, Fierro S, Hu X (2012) Fe, Co, and Ni ions promote the catalytic activity of amorphous molybdenum sulfide films for hydrogen evolution. Chem Sci 3:2515–2525

15. Yan Y, Xia B, Qi X, Wang H, Xu R, Wang J, Zhang H, Wang X (2013) Nano-tungsten carbide decorated graphene as co-catalysts for enhanced hydrogen evolution on molybdenum disulfide. Comm Common 49:4884–4886

16. Bonde J, Moses PG, Jaramillo TF, Norskov JK, Chorkendorff I (2009) Hydrogen evolution on nano-particulate transition metal sulfides. Faraday Discuss 140:219–231

17. Brorson M, Carlsson A, Topsøe H (2007) The morphology of MoS₂,WS₂, Co–Mo–S, Ni–Mo–S and Ni–W–S nanoclusters in hydrodesulfurization catalysts revealed by HAADF-STEM. Catal Today 123:31–36

18. Bouwens SMAM, Van Veen JAR, Koningsberger DC, De Beer VHJ, Prins R (1991) EXAFS determination of the structure of cobalt in carbon-supported cobalt and cobaltmolybdenum sulfide hydrodesulfurization catalysts. J Phys Chem 95:123–134

19. Yan Y, Xia BY, Xu ZC, Wang X (2014) Recent development of molybdenum sulfides as advanced electrocatalysts for hydrogen evolution reaction. ACS Catal 4:1693–1705

20. Ferrin P, Kandoi S, Zhang J, Adzic R, Mavrikakis M (2009) Molecular atomic hydrogen interactions with Au-Ir near-surface alloys. J Phys Chem C 113:1411–1417

21. Nørskov JK, Bligaard T, Logadottir A, Kitchin JR, Chen J, Pandelov S, Stimming U (2005) Trends in the exchange current for hydrogen evolution. J Electrochem Soc 152:J23–J26

22. Sun YJ, Liu C, Grauer DC, Yano J, Long JR, Yang P, Chang CJ (2013) Electrodeposited cobalt-sulfide catalyst for electrochemical and photoelectrochemical hydrogen generation from water. J Am Chem Soc 135:17699–17702

23. William S, Hummers JR, Richard EO (1958) Preparation of graphitic oxide. J Am Chem Soc 80:1339–1348

24. Xiao J, Wang XJ, Yang XQ, Xun SD, Liu G, Koech PK, Liu J, Lemmon JP (2011) Electrochemically induced high capacity displacement reaction of PEO/MoS₂/graphene nanocomposites with lithium. Adv Funct Mater 21:2840–2852

25. Merki D, Fierro S, Vrubel H, Hu X (2011) Amorphous molybdenum sulfide films as catalysts for electrochemical hydrogen production in water. Chem Sci 2:1262–1267

26. Liu KK, Zhang WJ, Lee YH, Lin YC, Chang MT, Su CY, Chang CS, Li H, Shi YM, Zhang H, Lai CS, Li LJ (2012) Growth of large-area and highly crystalline MoS₂ thin layers on insulating substrates. Nano Lett 12:1538–1544

27. Tan BJ, Klabunde KJ, Sherwood PMA (1991) XPS studies of solvated metal atom dispersed (SMAD) catalysts evidence for layered cobalt–manganese particles on alumina and silica. J. Am Chem Soc 113:855–861

28. Mclntyre NS, Cook MG (1975) X-ray photoelectron studies on some oxides and hydroxides of cobalt, nickel, and copper. Anal Chem 47:2208–2213

29. De Jong AM, De Beer VHJ, Van Veen JAR, Niemantsverdriet JW (1996) Surface science model of a working cobalt-promoted molybdenum sulfide hydrodesulfurization catalyst: characterization and reactivity. J Phys Chem 100:17722–17725

30. Giovanni C, Wang W, Nowak S, Greneche J, Lecoq H, Mouton L, Giraud M, Tard C (2014) Bioinspired iron sulfide nanoparticles for cheap and long-lived electrocatalytic molecular hydrogen evolution in neutral water. ACS Catal 4:681–687

31. Yu SJ, Jiang YM, Wang CM (2013) A polymer composite consists of electrochemical reduced grapheme oxide/polyimide/chemical reduced

graphene oxide for effective preparation of SnSe by electrochemical atomic layer deposition method with enhanced electrochemical performance and surface area. Electrochim Acta 114:430–438

32. Zhou KQ, Liu JJ, Shi YQ, Jiang SH, Wang D, Hu Y, Zhou G (2015) MoS$_2$ nanolayers grown on carbon nanotubes: an advanced reinforcement for epoxy composites. ACS Appl Mater Interfaces 7: 6070–6081

33. Anson FC (1964) Application of potentiostatic current integration to the study of the adsorption of cobalt(III)-(Ethylenedinitrilo(tetraacetate) on mercury electrodes. Anal Chem 36:932–934

34. Jaramillo TF, Jorgensen KP, Bonde J, Nielsen JH, Horch S, Chorkendorff I (2007) Identification of active edge sites for electrochemical H-2 evolution from MoS$_2$ nanocatalysts. Science 317:100–102

35. Ji S, Yang Z, Zhang Z, Liu Z, Tjiu WW, Phang IY, Zhang Z, Pan J, Liu T (2013) Exfoliated MoS$_2$ nanosheets as efficient catalysts for electrochemical hydrogen evolution. Electrochim Acta 109:269–275

36. Rowley-Neale SJ, Brownson DAC, Smith GC, Sawtell DAG, Kelly PJ, Banks CE (2015) 2D nanosheet molybdenum disulphide (MoS$_2$) modified electrodes explored towards the hydrogen evolution reaction. Nanoscale 7:18152–18168

37. Cui W, Ge CJ, Xing ZC, Asiri AM, Sun XP (2014) Ni$_x$S$_y$-MoS$_2$ hybrid microspheres: one-pot hydrothermal synthesis and their application as a novel hydrogen evolution reaction electrocatalyst with enhanced activity. Electrochim Acta 137:504–510